

# InvarDiff: Cross-Scale Invariance Caching for Accelerated Diffusion Models

Zihao Wu  
Peking University

zihawu25@stu.pku.edu.cn

<https://github.com/zihawu25/InvarDiff>

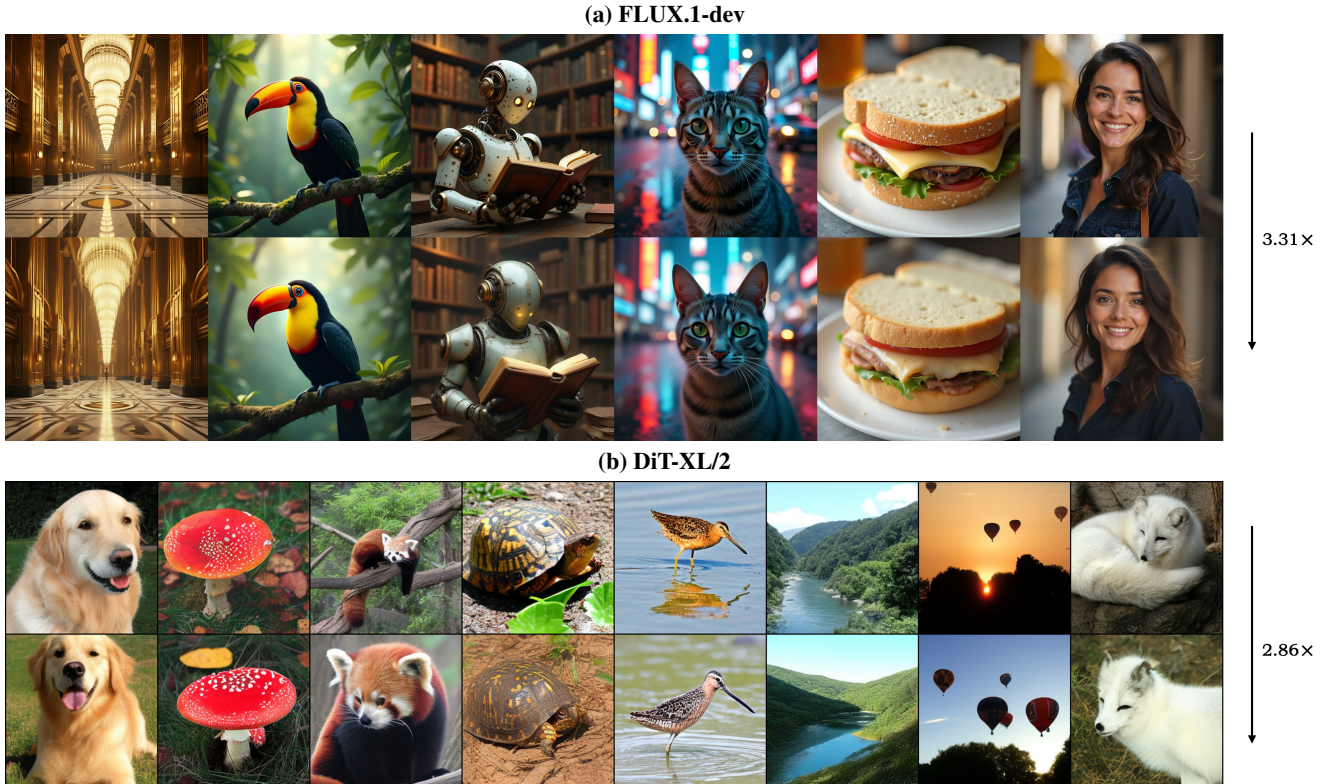


Figure 1. Our method achieves  $3.31\times$  speedup on FLUX.1-dev (A800, 28 steps) and  $2.86\times$  on DiT-XL/2 (RTX 4070S, 50 steps).

## Abstract

Diffusion models deliver high-fidelity synthesis but remain slow due to iterative sampling. We empirically observe there exists feature invariance in deterministic sampling, and present InvarDiff, a training-free acceleration method that exploits the relative temporal invariance across timestep-scale and layer-scale. From a few deterministic runs, we compute a per-timestep, per-layer, per-module binary cache plan matrix and use a re-sampling correction to avoid drift when consecutive caches occur. Using quantile-based change metrics, this matrix specifies which module at which step is reused rather than recomputed. The same invariance criterion is applied at the step scale to enable cross-timestep caching, deciding whether an entire step can reuse cached

results. During inference, InvarDiff performs step-first and layer-wise caching guided by this matrix. When applied to DiT and FLUX, our approach reduces redundant compute while preserving fidelity. Experiments show that InvarDiff achieves 2–3 $\times$  end-to-end speed-ups with minimal impact on standard quality metrics. Qualitatively, we observe almost no degradation in visual quality compared with full computations.

## 1. Introduction

Diffusion models have emerged as a leading approach to high-fidelity, controllable image and video generation [10–12, 28, 29, 31, 34], yet their iterative denoising makes infer-

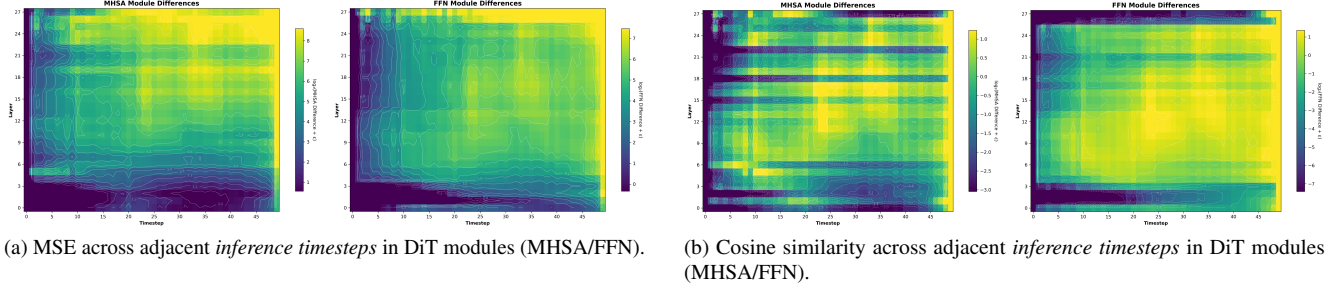


Figure 2. **Temporal invariance in DiT under 50-step sampling.** The horizontal axis is the *inference timestep* (the reverse-ordered timesteps), not the training diffusion time. For each layer  $l$  and timestep  $t > 0$ , the heatmaps show the change (**log2 scale**) between adjacent inference steps for  $s \in \{\text{MHSA}, \text{FFN}\}$ : (a)  $\text{MSE}(Z_{l,t}^{(s)}, Z_{l,t-1}^{(s)})$  and (b)  $\cos\angle(Z_{l,t}^{(s)}, Z_{l,t-1}^{(s)})$ . The first column ( $t=0$ ) is set to 0. Values are averaged over inputs from **10** distinct class labels; the per-(timestep, layer) patterns closely match single-class maps (see Appendix), supporting a global threshold for cache planning over (timestep, layer, module).

ence slow and costly. Each sample requires dozens to hundreds of sequential network evaluations of a large backbone (from U-Net to DiT models [27, 30]), and every evaluation invokes expensive modules such as multi-head self attention (MHSA) and feed-forward blocks (FFN) [38]. The strict stepwise dependency limits parallelism across timesteps, so latency scales roughly with the number of steps, while memory traffic and energy consumption grow accordingly. These factors hinder real-time or interactive applications (editing, content creation, serving at scale) and constrain deployment on resource-limited hardware. Consequently, there is a clear need for inference-time acceleration that preserves fidelity while reducing per-sample latency and cost. Main acceleration avenues for diffusion models can be grouped into three categories [47]: (1) fewer sampling steps; (2) cheaper per-step computation; (3) cache-based reuse across steps or layers.

Many methods speed up generation by reducing the number of denoising iterations. High-order or adaptive samplers (DDIM, DPM-Solver) recast sampling as an ODE to reach good quality in tens or even single-digit steps [21, 22, 35, 50]; distillation further shortens trajectories (Progressive Distillation; one-step Consistency Models) [32, 37], and Rectified Flow straightens the probability flow toward near one-step generation [7, 17, 20]. These gains come with trade-offs: slight fidelity degradation at very low step counts, heavy retraining cost, and modified teacher–student pipelines. A complementary axis lowers the per-step cost via model compression and efficient inference: quantization and pruning shrink DiT attention/FFN compute [4, 33, 41], while sparse attention mechanisms skip redundant computations [45, 46]. Token merging/dropping limits all-to-all interactions [2, 3], and system optimizations (memory scheduling, heterogeneous GPU/CPU deployment) further cut latency [6]. Such per-step methods typically require architectural or inference changes and tuning effort, but combine well with step-reduction for compounded speed-ups.

Beyond the above, a recent orthogonal idea is to exploit the redundancy in model computations across consecutive timesteps [19]. Since adjacent diffusion steps operate on gradually denoised inputs, their intermediate activations often overlap significantly. Emerging works leverage this by caching and reusing computations from one step in the next [5, 14, 18, 23, 25, 26, 43, 51]. For instance, some approaches reuse feature maps from the previous timestep’s DiT forward pass to avoid recomputation [23, 51], while others skip entire Transformer blocks on selected steps under change-based criteria. In addition to timestep-adaptive reuse, a complementary strategy is layer-adaptive reuse within a step [1, 24, 43]. This enables savings even when an entire step cannot be skipped and provides fine-grained control over where compute is spent.

We consider conditional DiT image generation, where at timestep  $t$  the model consumes a noisy latent  $x_t$  together with a class-label embedding  $y$  (classifier-free guidance [9] is used). Under deterministic samplers including DDIM with  $\eta = 0$ , DPM-Solver, and flow/rectified-flow ODE solvers [17, 20–22, 35], the transition  $x_t \rightarrow x_{t-1}$  injects no stochastic noise [36], so internal activations can be tracked across steps; in contrast, SDE samplers such as DDPM [10] add randomness at every step and are outside our scope. DiT processes images (or VAE latents) as sequences of patch tokens: the input is partitioned into non-overlapping patches and linearly projected to token embeddings, upon which Transformer blocks (MHSA/FFN) operate [27, 29]. We quantify temporal invariance with two complementary measures at each layer  $l$  and module  $s \in \{\text{MHSA}, \text{FFN}\}$ :  $\text{MSE}(Z_{l,t}^{(s)}, Z_{l,t-1}^{(s)})$  to capture magnitude/energy changes, and  $\cos\angle(Z_{l,t}^{(s)}, Z_{l,t-1}^{(s)})$  to capture directional changes of token representations; the first step is set to 0. Figure 2 (50-step deterministic sampling) aggregates results over 10 distinct class labels and closely matches single-class maps (Appendix), indicating a two-scale invariance pattern across timesteps and across layers/modules. DiT variants (for ex-

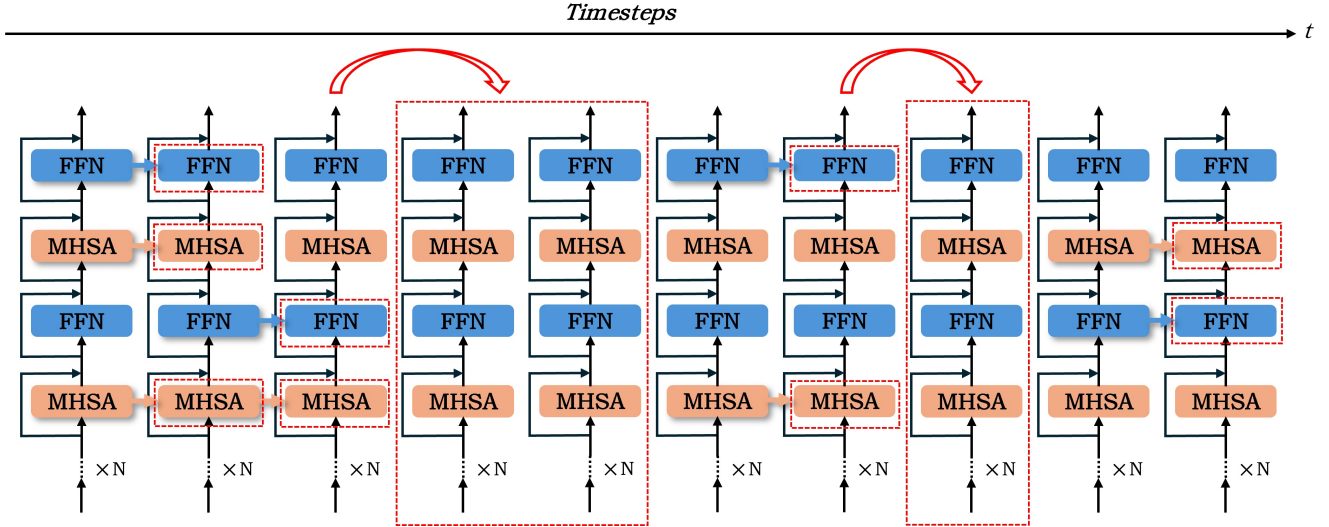


Figure 3. Cross-scale caching schematic. We exploit two scales of reuse: (i) **across timesteps** (step-level reuse) and (ii) **within a timestep across modules** (layer-wise reuse of MHSA/FFN). The scheduler first tests a step-level gate; if reuse is unsafe, it traverses layers and selectively reuses or recomputes modules according to the cache plan. Dashed boxes indicate reused modules; red arcs depict cross-timestep reuse.

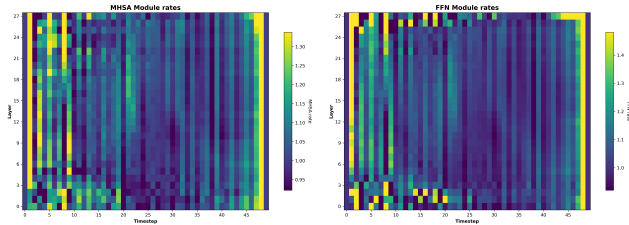


Figure 4. Average rate matrices  $\rho$  (MHSA/FFN) over 10 class labels. The horizontal axis denotes *inference timesteps* (test-time sampling from  $t$  to  $t-1$ ), not the training diffusion time. The first and the last timestep are set to 1 for visualization. Axes: *Timestep* ( $x$ ) and *Layer* ( $y$ ). See §3 for the definition of  $\rho$ .

ample FLUX [16]) share MHSA/FFN building blocks and often adopt ODE-based [36] deterministic sampling, so this principle is structurally applicable to that family, including DiT-style video generators [15, 40, 44, 48, 52].

Building on this observation, we propose InvarDiff, a training-free scheme that plans and executes reuse at two scales. From a small deterministic calibration, we compute simple feature-change statistics and, using quantile thresholds, derive a binary cache plan  $C \in \{0, 1\}^{T \times L \times S}$  over  $(t, l, s)$  with  $S = \{\text{MHSA}, \text{FFN}\}$ ; the same criterion is aggregated to a step-level flag  $c_t^{\text{step}}$  that decides when an entire step can reuse cached results. We use both scales because temporal invariance is heterogeneous across timesteps and depth. A step-level gate therefore captures intervals where a full forward pass can be safely reused and yields large, predictable savings; when whole-step reuse is unsafe, many modules inside the step are still near-invariant, so a layer-

/module-level planner can recover substantial compute by reusing their cached outputs. We also include a calibration-time resampling correction to refine the cache plan. At inference, we follow a step-first then layer-wise schedule guided by the final plan  $C$ . This design is orthogonal to sampler improvements and per-step efficiency techniques, and targets DiT/DiT-variant generators [16, 27].

## 2. Related Work

### 2.1. Diffusion Models

Diffusion probabilistic models [10] are a leading paradigm for high-quality image and video synthesis. Early systems relied on convolutional U-Net backbones [30], achieving strong image and initial video results [12, 29] but facing scalability limits. Transformer-based Diffusion Transformers (DiT) [27] replace U-Net, capture long-range dependencies, and now serve as backbones for state-of-the-art text-to-video generators [15, 40, 44, 48, 52]. Despite these advances, diffusion models remain compute-intensive, requiring dozens to hundreds of denoising steps through large networks. This leads to slow sampling and high inference cost, which motivates acceleration.

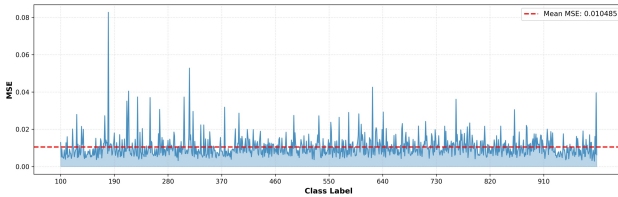
### 2.2. Cache-Based Acceleration

A first line of work reduces the number of steps using advanced samplers or distillation: DDIM, ODE solvers such as DPM-Solver and UniPC [21, 22, 35, 36, 50]; training-based step reduction (progressive distillation) cuts steps but requires retraining [32], while training-free solvers avoid retraining yet can degrade at very low step counts. A second

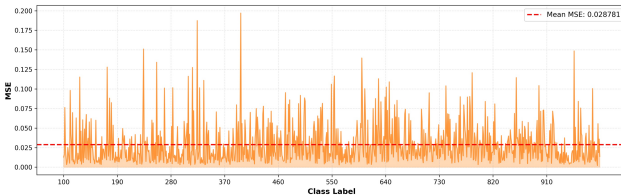
line lowers per-step cost via model compression or quantization [4, 33, 41], often needing fine-tuning and architectural changes.

In contrast, caching provides a training-free alternative by reusing computations across timesteps when changes are small [19]. DeepCache [25] caches high-level U-Net features; in video, Pyramid Attention Broadcast [51] reuses multi-scale attention context. For transformer-based diffusion, methods include AdaCache, TeaCache, MagCache, and FasterCache [14, 18, 23, 26]. Despite notable gains, many approaches still require non-trivial adjustments to preserve quality, and acceleration for DiT-based models remains limited, especially at high resolution or long video length, motivating specialized caching and skipping strategies for transformer diffusion.

### 3. Methodology



(a) MHSA modules — cross-class MSE to the reference rate matrix (classes 0–99 averaged).



(b) FFN modules — cross-class MSE to the reference rate matrix (classes 0–99 averaged).

Figure 5. Cross-class stability of the rate matrices  $\rho$ . Using DiT class labels 0–99 to form a reference rate matrix  $R_{\text{ref}}^{(s)}$  for each module  $s \in \{\text{MHSA}, \text{FFN}\}$ , we compute  $\text{MSE}(R_c^{(s)}, R_{\text{ref}}^{(s)})$  for  $c = 100, \dots, 999$  (DiT class labels on the  $x$ -axis). As shown in Fig. 4, most entries of  $\rho$  lie in the 0.9–1.5 band, and the curves here remain low and flat, indicating that (timestep, layer) patterns of  $\rho$  are largely class-independent. This supports using a single global quantile threshold to derive a binary cache plan.

#### 3.1. Setting and Notation

We study conditional generation with DiT-family backbones, including class-conditioned DiT and text-conditioned FLUX. At inference timestep  $t \in \{0, \dots, T-1\}$  the model takes a noisy latent  $x_t$  and a conditioning embedding  $y$ , and uses classifier-free guidance. Images or VAE latents are represented as sequences of patch tokens. Let  $L$  be the number of Transformer blocks and let  $S = \{\text{MHSA}, \text{FFN}\}$  denote the submodules in each block. We write  $Z_{l,t}^{(s)} \in \mathbb{R}^{N \times d}$  for the output of submodule  $s \in S$  at layer  $l$  and timestep  $t$ , and

$z_t \in \mathbb{R}^{N \times d}$  for the network output before VAE decoding. From a small deterministic calibration set we will build a binary cache-plan matrix  $C \in \{0, 1\}^{T \times L \times |S|}$  and a step-level gate  $c_t^{\text{step}} \in \{0, 1\}$ .

#### 3.2. Empirical Invariance and Metrics

Deterministic sampling yields highly correlated activations across adjacent inference timesteps. We quantify temporal change for each layer  $l$  and submodule  $s \in S$  with two complementary quantities:  $\text{MSE}(Z_{l,t}^{(s)}, Z_{l,t-1}^{(s)})$  captures magnitude variation, while  $\cos \angle(Z_{l,t}^{(s)}, Z_{l,t-1}^{(s)})$  captures directional consistency of token representations; see Fig. 2.

For planning we use a layer/module change *rate* that compares two consecutive first-order differences:

$$\rho_{l,t}^{(s)} = \frac{\|Z_{l,t+1}^{(s)} - Z_{l,t}^{(s)}\|_1}{\|Z_{l,t}^{(s)} - Z_{l,t-1}^{(s)}\|_1}. \quad (1)$$

This emphasizes stretches where updates shrink over time.

We also measure a step-level rate using the network output  $z_t$ :

$$\rho_t^{(\text{net})} = \frac{\|z_{t+1} - z_t\|_1}{\|z_t - z_{t-1}\|_1}. \quad (2)$$

Boundary timesteps follow the same handling as in our implementation. Averaging these statistics over a small set of inputs reveals stable two-scale patterns across timesteps and layers (Fig. 4); class-wise stability curves further support the use of global quantile thresholds (Fig. 5).

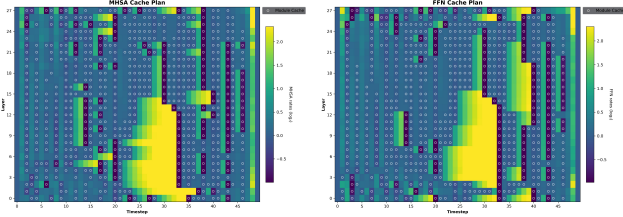
#### 3.3. Two-Phase Calibration

We estimate a reuse plan from a small deterministic calibration set  $\mathcal{D}$ , without any retraining. The plan consists of a per-step gate  $c_t^{\text{step}} \in \{0, 1\}$  and a per-(timestep, layer, module) matrix  $C \in \{0, 1\}^{T \times L \times |S|}$ . All decisions are derived from the rates in §3.2.

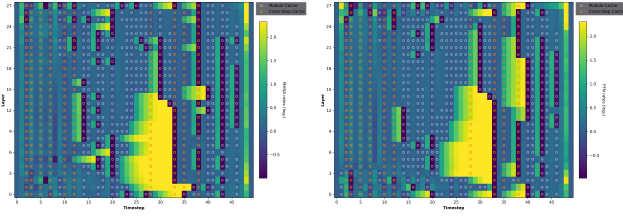
**Phase 1: initial plan.** Run a few deterministic trajectories on  $\mathcal{D}$  and record  $Z_{l,t}^{(s)}$  and  $z_t$  for all  $t$  and  $l$ . Compute  $\rho_{l,t}^{(s)}$  and  $\rho_t^{(\text{net})}$  and pool them over  $\mathcal{D}$ . Choose fixed quantile thresholds  $(\tau_{\text{MHSA}}, \tau_{\text{FFN}}, \tau_{\text{step}})$  and set the initial binary plan  $C^{(0)}$  and step gates  $c^{(0)}$ . For safety, the first step and the final step are forced to compute.

**Phase 2: resampling correction.** Using the same calibration set  $\mathcal{D}$  as in Phase 1 (identical class labels/prompts and fixed seeds), we re-run the model without skipping any computation and measure rates under simulated consecutive reuse. The two scales are corrected separately at the same time:

Layer-wise correction applies the initial layer plan  $C^{(0)}$ . During the forward pass we still compute every module,



(a) Resampling correction with  $\text{step-th}=0.00$  and  $\text{MHSA/FFN-th}=0.50$ . Background denotes the post-resampling  $\log_2 \rho$ ; white circles mark layer/module caches. Consecutive reuse makes  $\rho$  larger (yellow regions).



(b) Enabling cross-step caching with  $\text{step-th}=0.20$  ( $\tau_{\text{MHSA}} = \tau_{\text{FFN}} = 0.50$ ). Orange circles mark step-level caches; white circles mark layer/module caches. The distribution of step-level caches differs from layer-level ones, showing their complementarity.

Figure 6. Effect of resampling correction and the combination of cross-step and layer-wise caching on DiT. Background colors visualize  $\log_2 \rho$  after resampling; dots indicate which computations are reused.

but for the cache state and for rate evaluation we replace  $Z_{l,t}^{(s)}$  with the cached  $Z_{l,t-1}^{(s)}$  whenever  $C^{(0)}[t, l, s]=1$ . This yields chained-reuse rates  $\rho_{l,t}^{(s)}$ ; thresholding them with the same quantiles yields the refined layer plan  $\tilde{C}$ .

Step-level correction applies the initial step gate  $c^{(0)}$ . We again run full forwards; for rate evaluation we replace  $z_t$  with  $z_{t-1}$  whenever  $c_t^{(0)}=1$ , simulating chained step reuse. Thresholding the resulting  $\rho_t^{(\text{net})}$  produces the refined step gate  $\tilde{c}^{\text{step}}$ .

Finally we fix  $C \leftarrow \tilde{C}$  and  $c^{\text{step}} \leftarrow \tilde{c}^{\text{step}}$  for inference. No layer or timestep is skipped during these calibration re-runs, only the tensors used for rate computation and cache updates are replaced according to the simulated policy.

**Analysis.** In Fig. 6, the heatmaps visualize post-resampling  $\log_2 \rho$  averaged over 12 DiT class labels. Figure 6(a) shows the case with the step gate disabled. White circles denote module caches chosen by the initial thresholds, while the background shows the rates recomputed under consecutive reuse. Many cached bands turn yellow, meaning  $\rho$  grows once reuse is chained. The resampling correction therefore pushes these units above the quantile thresholds and flips them back to compute, leaving a sparser set of caches concentrated in genuinely stable regions (typically late steps and several middle-layer bands). This explains why a second pass is necessary: it removes false positives that would otherwise accumulate error.

Figure 6(b) enables the step gate ( $\tau_{\text{step}}=0.20$ ). Orange circles mark whole-step caches and exhibit a pattern different from the layer-wise ones: step-level reuse appears in contiguous time intervals even when some layers remain active, whereas layer-wise reuse stays localized to specific MHSA/FFN bands. The two scales are thus complementary—step gates capture long near-constant intervals for large savings, and layer-wise gates recover additional redundancy inside the remaining steps. Together, the corrected plan yields reliable reuse decisions and a better speed-quality trade-off than either scale alone.

### 3.4. Inference-time scheduling

At test time the fixed plan  $(C, c^{\text{step}})$  is followed verbatim, with no adaptation. For iteration  $t$ , first consult  $c_t^{\text{step}}$ . If  $c_t^{\text{step}}=1$ , skip the entire forward pass at step  $t$  and set  $z_t \leftarrow z_{t-1}$ ; cached submodule tensors are implicitly valid for this step. If  $c_t^{\text{step}}=0$ , execute step  $t$  while applying the layer/module plan: for each layer  $l$ , reuse the MHSA output when  $C[t, l, \text{MHSA}]=1$  and otherwise compute it and overwrite the cache; then apply the same rule to FFN using  $C[t, l, \text{FFN}]$ . Newly computed outputs always update the cache. After a step-level reuse at  $t$ , we mask all layer-level caches at  $t+1$  once to avoid stale cross-step chaining.

This joint step gate and layer-wise gating captures long intervals where the whole step can be reused, and still reduces cost inside steps where only a subset of modules changes. Because the schedule is precomputed, latency is predictable and quality remains close to the full computation.

### 3.5. Adapting to FLUX and DiT-style variants

FLUX [16] follows the same Transformer backbone pattern as DiT, so the invariance measures in §3.2 transfer directly. We keep the step state  $z_t$  and the layer tensors  $Z_{l,t}^{(s)}$  from §3.1 and only adapt the module families and threshold tying.

**Module families.** FLUX has dual-stream blocks (image and context/text) and single-stream blocks. We cache at the level of families and use one step gate shared by both streams:

$$S_{\text{FLUX}} = \{\text{dual\_attn}, \text{dual\_ff}, \text{dual\_context\_ff}, \text{single\_attn}, \text{single\_ff}\}. \quad (3)$$

Here `dual_attn` denotes the attention family in dual-stream blocks and governs both the image self-attention and the context/text attention (formerly `dual_context_attn`); `dual_ff` is the image-stream feed-forward in dual-stream blocks; `dual_context_ff` is the context-stream feed-forward; `single_attn` and `single_ff` are the attention and feed-forward in single-stream blocks. Each family  $s \in S_{\text{FLUX}}$  yields its own  $Z_{l,t}^{(s)}$  and is cached independently.



Figure 7. Qualitative comparison on FLUX.1-dev. Rows on the right indicate the method and its measured end-to-end speedup; each column corresponds to one prompt. Our approach significantly improved the acceleration ratio while maintaining high visual fidelity. All images are  $1024 \times 1024$ .

**Calibration.** We reuse the two-phase procedure in §3.3. On a small set of fixed prompts and seeds, we compute  $\rho_{l,t}^{(s)}$  for all  $s \in S_{\text{FLUX}}$  and the step-level rate  $\rho_t^{(\text{net})}$ . Quantile thresholds are chosen per family, with a shared attention threshold applied to both dual-stream attentions:

$$\tau_{\text{FLUX}} = \{\tau_{\text{dual\_attn}}, \tau_{\text{dual\_ff}}, \tau_{\text{dual\_context\_ff}}, \tau_{\text{single\_attn}}, \tau_{\text{single\_ff}}, \tau_{\text{step}}\}. \quad (4)$$

Phase 2 resampling on the same prompts refines  $C^{(0)}, c^{(0)}$  to the final  $C, c^{\text{step}}$ . The step gate is computed from the unified  $z_t$  (output before VAE decoding), so both streams share the same step-level decision.

**Inference.** The scheduler in §3.4 is used as is. If  $c_t^{\text{step}}=1$ , both streams reuse the previous state and the whole step is skipped. Otherwise, for each layer  $l$  and family  $s \in S_{\text{FLUX}}$ , reuse  $Z_{l,t-1}^{(s)}$  when  $C[t,l,s]=1$  and recompute it when  $C[t,l,s]=0$ . For dual-stream attention blocks, the single entry  $C[t,l,\text{dual\_attn}]$  governs both image and context attentions.

**Practical notes.** Features are collected via forward hooks for each family and pooled over tokens to a single scalar for each  $(t,l,s)$ . We run a short warm-up at the beginning where the first few steps are computed in full, and the final step is also executed without reuse to secure fidelity. On an NVIDIA A800, the two-phase calibration using five prompts for averaging completes in only **about two minutes** of wall-clock time. The resulting cache plan is reused across

seeds, prompts, and runs. The same recipe extends to other DiT-based image and video generators by enumerating their attention and FFN families, tying attention thresholds when appropriate, and then running the same two-phase calibration and the same runtime schedule.

## 4. Experiment

### 4.1. Settings

We evaluate on two backbones. FLUX.1-dev generates  $1024 \times 1024$  images with  $T=28$  steps on an NVIDIA A800 80GB. DiT-XL/2 generates  $256 \times 256$  images with  $T=50$  steps on an NVIDIA RTX 4070S 12GB [39]. We adopt the same deterministic sampling procedure as the full-compute baseline. Speedup and latency are measured end to end against the full model, including the VAE decode. Compute is reported as FLOPs(P) for FLUX and FLOPs(T) for DiT to reflect per-pass cost. Quality is measured by LPIPS  $\downarrow$ , SSIM  $\uparrow$ , and PSNR  $\uparrow$  [13, 42, 49], computed against each backbone’s full deterministic reference under the same prompts and labels, with DiT compared to its DDIM reference and FLUX compared to its default flow sampler reference.

For data, FLUX is evaluated on 100 GenEval[8] prompts, one image per prompt; DiT is evaluated on 500 ImageNet class labels, one image per label. All metrics are averaged over the corresponding set. Our calibration uses a small deterministic subset from these sources to produce a fixed plan used at inference (5 prompts for FLUX and 16 class labels for DiT).

Table 1. Quantitative evaluation of inference efficiency and visual quality. FLUX images are  $1024 \times 1024$ ; DiT images are  $256 \times 256$ . **Setup.** For **FLUX.1-dev** we evaluate on an NVIDIA A800-80GB using 100 prompts from GenEval[8]; each prompt renders a  $1024 \times 1024$  image and metrics are averaged. For **DiT-XL/2** we evaluate on an NVIDIA RTX 4070S-12GB using 500 class labels; each label renders a  $256 \times 256$  image and metrics are averaged. Speedup is measured end-to-end against the full baselines. *Learning-to-Cache* is the NeurIPS 2024 method included for comparison. Our method attains up to  $3.31 \times$  on FLUX and  $2.86 \times$  on DiT while maintaining visual quality. The two operating points (fast/slow) expose a wider, tunable speed–fidelity range than prior caching baselines.

Method	Efficiency			Visual Quality		
	FLOPs (P) ↓	Speedup ↑	Latency (s) ↓	LPIPS ↓	SSIM ↑	PSNR ↑
<b>FLUX.1-dev</b> ( $T = 28, 1024 * 1024$ )						
FLUX.1-dev[16]	1.67	1×	14.75	—	—	—
TeaCache ( $\delta=0.6$ )[18]	0.71	2.465×	5.98	0.3472	0.7250	18.2024
MagCache (fast)[26]	0.53	2.945×	5.01	0.2579	0.7813	21.0270
MagCache (slow)[26]	0.60	2.471×	5.97	0.1980	0.8163	23.0826
<b>Ours (fast)</b>	0.54	<b>3.315×</b>	<b>4.45</b>	0.3286	0.7255	19.3550
<b>Ours (slow)</b>	0.83	2.477×	5.96	<b>0.1562</b>	<b>0.8549</b>	<b>25.4561</b>
<b>DiT-XL/2</b> ( $T = 50, 256 * 256$ )						
	FLOPs (T) ↓	Speedup ↑	Latency (s) ↓	LPIPS ↓	SSIM ↑	PSNR ↑
DDIM[35]	22.89	1×	8.12	—	—	—
Learning-to-Cache[24]	14.19	1.275×	6.37	<b>0.6854</b>	0.2316	9.1293
<b>Ours (fast)</b>	7.96	<b>2.860×</b>	<b>2.84</b>	0.6892	0.2264	<b>9.6487</b>
<b>Ours (slow)</b>	8.82	2.567×	3.17	0.6936	<b>0.2449</b>	9.5219

## 4.2. Baselines

We compare to widely used caching and skipping methods under matched samplers and guidance. Full model of each backbone serves as the reference. TeaCache selects cacheable steps from timestep embeddings. MagCache provides two operating points (fast and slow) driven by residual magnitude. Learning-to-Cache (NeurIPS 2024) trains a policy router for DiT. All baselines run with their public configurations; we keep step counts and precision identical.

## 4.3. Main results

**Quantitative.** Table 1 summarizes efficiency and visual quality. On FLUX.1-dev (A800), our method attains up to  $3.31 \times$  end-to-end acceleration (Ours fast) with competitive perceptual quality, and a higher-fidelity operating point at  $2.48 \times$  (Ours slow) that yields the best LPIPS, SSIM, and PSNR in the table. Both operating points reduce compute markedly relative to the full model and are consistently stronger than TeaCache at similar speeds. On DiT-XL/2 (4070S), our method reaches  $2.86 \times$  with comparable LPIPS/SSIM to Learning-to-Cache and higher PSNR, while cutting FLOPs(T) from 22.89 to 7.96. This is more than  $2.2 \times$  the speedup of Learning-to-Cache ( $1.275 \times$ ). A slower variant at  $2.57 \times$  further improves fidelity.

**Qualitative.** Fig. 1 shows side-by-side generations across prompts and classes. The FLUX comparison in Fig. 7 illustrates that our reuse preserves textures and structure while

achieving a larger speed gain than TeaCache and MagCache. Overall, the two operating points expose a wider, tunable speed–quality range than prior caching baselines, with predictable latency from the fixed schedule.

## 4.4. Ablation Studies

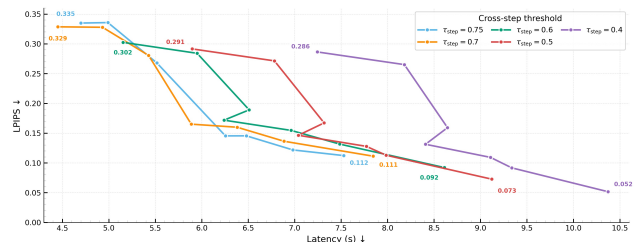


Figure 8. Speed–Quality tradeoff on FLUX.1-dev (A800,  $T=28$ ). Each point shows latency and LPIPS for one operating point (35 total, calibration averages 5 prompts). Each polyline fixes  $\tau_{\text{step}} \in \{0.40, 0.50, 0.60, 0.70, 0.75\}$  and sweeps seven preset threshold bundles. A bundle is  $(\tau_{\text{warm-up}}, \tau_{\text{dual.attn}}, \tau_{\text{dual.ff}}, \tau_{\text{dual.context.ff}}, \tau_{\text{single.attn}}, \tau_{\text{single.ff}})$ . Bundle order is aligned across polylines, only  $\tau_{\text{step}}$  changes.

**Cross-timestep and cross-layer reuse.** Figure 9 visualizes how module-wise and total skip correlate with runtime across operating points on FLUX.1-dev. As total reuse increases, latency drops, and faster operating points exhibit stronger reuse on attention pathways. At matched visual quality, the two scales contribute differently. On DiT-XL/2, using only

the step gate or only the layer/module gate yields speedups just above  $2\times$ , whereas using both simultaneously reaches  $2.86\times$ . On FLUX, layer-only reuse reaches about  $1.5\times$ , and combining step and layer reuse exceeds  $3\times$ . These results indicate complementary roles: the step gate captures long near-constant intervals, while the layer-wise gate trims residual redundancy within active steps.

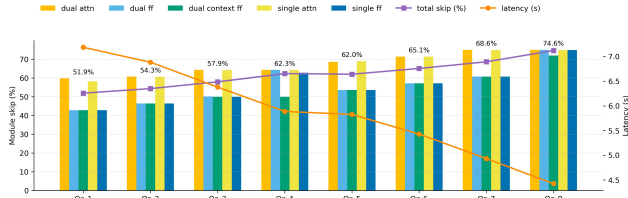


Figure 9. Module-wise skip and latency across operating points (Op- $\{k\}$ ) on FLUX.1-dev. Bars show per-module skip ratios (dual\_attn, dual\_ff, dual\_context\_ff, single\_attn, single\_ff).

**Resampling correction.** Resampling correction recalibrates the plan under simulated consecutive reuse. Without this second pass, chained reuse can make the measured change rates overly optimistic, which leads to local distortions and structural drift at the same thresholds. Resampling correction removes such false positives, stabilizes the cached trajectory, and yields clearly better visual quality at the same acceleration or higher acceleration at comparable quality.

**Sensitivity to thresholds.** Within the redundancy regime, moderate threshold changes have limited impact on quality, with attention thresholds offering the most headroom. Excessive MHSA thresholds (e.g.,  $> 0.8$ ) can distort spatial layout, while overly high FFN thresholds degrade textures and introduce speckles. Raising the step threshold directly trades speed for quality and makes outcomes less sensitive to the per-module settings. On FLUX, dual/single attention is tolerant, lowering the single-stream FFN threshold reduces visible patch edges after upscaling. When the step threshold is small, pushing dual-stream FFN too high can cause speckles. A small warm-up threshold helps FLUX avoid early-step blur; for DiT it is negligible (set to 0).

Figure 8 summarizes the joint effect on FLUX.1-dev: it plots latency ( $x$ ) versus LPIPS ( $y$ ) for 35 operating points. Each polyline fixes a cross-step threshold ( $\tau_{\text{step}} \in \{0.40, 0.50, 0.60, 0.70, 0.75\}$ ) and sweeps seven preset module-threshold bundles (warm-up and five module thresholds). The curves are monotonic and outline a Pareto front: larger  $\tau_{\text{step}}$  yields lower latency at similar LPIPS, while tightening module thresholds moves points along a given polyline. A mild knee appears around 6–8s, and gains beyond this region require disproportionately more latency. These observations align with the above qualitative notes,

with the step threshold mainly controlling overall aggressiveness and the module thresholds shaping the residual speed-quality trade-off within active steps.

**Stability across classes and prompts.** Fig. 5 discusses the stability of the module-wise rate matrices across classes. The cache plan generalizes across class labels, prompts, and seeds. As shown in Tables 2 and 3, averaging over a small calibration set is sufficient: using about 10–20 labels for DiT and 5–10 prompts for FLUX already yields stable quality, with larger calibration sets providing negligible gains. The resulting plan also transfers to unseen labels/prompts and different random seeds.

Table 2. Effect of the number of class labels used in calibration on DiT-XL/2. Mean latency at this operating point is 2.997 s ( $T=50$ ).

# Class labels $K$	LPIPS $\downarrow$	SSIM $\uparrow$	PSNR $\uparrow$
1	0.6767	0.2085	9.6213
3	0.6832	0.2546	9.5933
5	0.6923	0.2535	9.5090
10	0.6874	0.2407	9.6129
15	0.6854	0.2353	9.5666
20	0.6844	0.2388	9.5937
30	0.6790	0.2350	9.5930

Table 3. Effect of the number of prompts used in calibration on FLUX.1-dev. Mean latency at this operating point is 5.662 s ( $T=28$ ).

# Prompts $K$	LPIPS $\downarrow$	SSIM $\uparrow$	PSNR $\uparrow$
1	0.2354	0.8242	22.2147
3	0.2813	0.8013	21.4066
5	0.2808	0.8005	21.4078
10	0.2368	0.8237	22.2213
15	0.2656	0.8051	21.4504
20	0.2655	0.8051	21.4505
30	0.2357	0.8245	22.2202

## 5. Conclusion

We presented *InvarDiff*, a training-free, cross-scale caching scheme for DiT-family diffusion generators. We leverage relative feature invariance to obtain a deterministic cross-scale caching policy. It offers complementary savings, requires no retraining or architectural changes, and composes with samplers, quantization, pruning, and systems optimizations. Experiments on DiT-XL/2 and FLUX.1-dev show substantial speedups with minimal quality impact, and the recipe transfers to DiT-style variants for efficient high-resolution image/video generation. Future work includes adaptive on-line plan updates, coupling with step-reduction or distillation, scaling the analysis to long-horizon video models, and making the cache plan self-adaptive to varying timestep schedules and lengths.

## References

- [1] Muhammad Adnan, Nithesh Kurella, Akhil Arunkumar, and Prashant J. Nair. Foresight: Adaptive layer reuse for accelerated and high-quality text-to-video generation, 2025. 2
- [2] Daniel Bolya and Judy Hoffman. Token merging for fast stable diffusion. In *Proceedings of the IEEE/CVF conference on computer vision and pattern recognition*, pages 4599–4603, 2023. 2
- [3] Daniel Bolya, Cheng-Yang Fu, Xiaoliang Dai, Peizhao Zhang, Christoph Feichtenhofer, and Judy Hoffman. Token merging: Your vit but faster. *arXiv preprint arXiv:2210.09461*, 2022. 2
- [4] Thibault Castells, Hyoung-Kyu Song, Bo-Kyeong Kim, and Shinkook Choi. Ld-pruner: Efficient pruning of latent diffusion models using task-agnostic insights. In *Proceedings of the IEEE/CVF Conference on Computer Vision and Pattern Recognition*, pages 821–830, 2024. 2, 4
- [5] Pengtao Chen, Mingzhu Shen, Peng Ye, Jianjian Cao, Chongjun Tu, Christos-Savvas Bouganis, Yiren Zhao, and Tao Chen.  $\delta$ -dit: A training-free acceleration method tailored for diffusion transformers. *arXiv preprint arXiv:2406.01125*, 2024. 2
- [6] Tri Dao, Dan Fu, Stefano Ermon, Atri Rudra, and Christopher Ré. Flashattention: Fast and memory-efficient exact attention with io-awareness. *Advances in neural information processing systems*, 35:16344–16359, 2022. 2
- [7] Patrick Esser, Sumith Kulal, Andreas Blattmann, Rahim Entezari, Jonas Müller, Harry Saini, Yam Levi, Dominik Lorenz, Axel Sauer, Frederic Boesel, et al. Scaling rectified flow transformers for high-resolution image synthesis. In *Forty-first international conference on machine learning*, 2024. 2
- [8] Dhruva Ghosh, Hanna Hajishirzi, and Ludwig Schmidt. General: An object-focused framework for evaluating text-to-image alignment, 2023. 6, 7
- [9] Jonathan Ho and Tim Salimans. Classifier-free diffusion guidance, 2022. 2
- [10] Jonathan Ho, Ajay Jain, and Pieter Abbeel. Denoising diffusion probabilistic models. *Advances in neural information processing systems*, 33:6840–6851, 2020. 1, 2, 3
- [11] Jonathan Ho, William Chan, Chitwan Saharia, Jay Whang, Ruiqi Gao, Alexey Gritsenko, Diederik P Kingma, Ben Poole, Mohammad Norouzi, David J Fleet, et al. Imagen video: High definition video generation with diffusion models. *arXiv preprint arXiv:2210.02303*, 2022.
- [12] Jonathan Ho, Tim Salimans, Alexey Gritsenko, William Chan, Mohammad Norouzi, and David J Fleet. Video diffusion models. *arXiv:2204.03458*, 2022. 1, 3
- [13] Alain Horé and Djemel Ziou. Image quality metrics: Psnr vs. ssim. In *2010 20th International Conference on Pattern Recognition*, pages 2366–2369, 2010. 6
- [14] Kumara Kahatapitiya, Haozhe Liu, Sen He, Ding Liu, Menglin Jia, Chenyang Zhang, Michael S Ryoo, and Tian Xie. Adaptive caching for faster video generation with diffusion transformers. In *Proceedings of the IEEE/CVF International Conference on Computer Vision*, pages 15240–15252, 2025. 2, 4
- [15] Weijie Kong, Qi Tian, Zijian Zhang, Rox Min, Zuozhuo Dai, Jin Zhou, Jiangfeng Xiong, Xin Li, Bo Wu, Jianwei Zhang, et al. Hunyuanvideo: A systematic framework for large video generative models. *arXiv preprint arXiv:2412.03603*, 2024. 3
- [16] Black Forest Labs, Stephen Batifol, Andreas Blattmann, Frederic Boesel, Saksham Consul, Cyril Diagne, Tim Dockhorn, Jack English, Zion English, Patrick Esser, Sumith Kulal, Kyle Lacey, Yam Levi, Cheng Li, Dominik Lorenz, Jonas Müller, Dustin Podell, Robin Rombach, Harry Saini, Axel Sauer, and Luke Smith. Flux.1 kontext: Flow matching for in-context image generation and editing in latent space, 2025. 3, 5, 7
- [17] Yaron Lipman, Ricky TQ Chen, Heli Ben-Hamu, Maximilian Nickel, and Matt Le. Flow matching for generative modeling. *arXiv preprint arXiv:2210.02747*, 2022. 2
- [18] Feng Liu, Shiwei Zhang, Xiaofeng Wang, Yujie Wei, Haonan Qiu, Yuzhong Zhao, Yingya Zhang, Qixiang Ye, and Fang Wan. Timestep embedding tells: It’s time to cache for video diffusion model. In *Proceedings of the Computer Vision and Pattern Recognition Conference*, pages 7353–7363, 2025. 2, 4, 7
- [19] Jiacheng Liu, Xinyu Wang, Yuqi Lin, Zhikai Wang, Peiru Wang, Peiliang Cai, Qinming Zhou, Zhengang Yan, Zexuan Yan, Zhengyi Shi, Chang Zou, Yue Ma, and Linfeng Zhang. A survey on cache methods in diffusion models: Toward efficient multi-modal generation, 2025. 2, 4
- [20] Xingchao Liu, Chengyue Gong, and Qiang Liu. Flow straight and fast: Learning to generate and transfer data with rectified flow. *arXiv preprint arXiv:2209.03003*, 2022. 2
- [21] Cheng Lu, Yuhao Zhou, Fan Bao, Jianfei Chen, Chongxuan Li, and Jun Zhu. Dpm-solver: A fast ode solver for diffusion probabilistic model sampling in around 10 steps. *Advances in neural information processing systems*, 35:5775–5787, 2022. 2, 3
- [22] Cheng Lu, Yuhao Zhou, Fan Bao, Jianfei Chen, Chongxuan Li, and Jun Zhu. Dpm-solver++: Fast solver for guided sampling of diffusion probabilistic models. *Machine Intelligence Research*, 22(4):730–751, 2025. 2, 3
- [23] Zhengyao Lv, Chenyang Si, Junhao Song, Zhenyu Yang, Yu Qiao, Ziwei Liu, and Kwan-Yee K. Wong. Fastercache: Training-free video diffusion model acceleration with high quality, 2025. 2, 4
- [24] Xinyin Ma, Gongfan Fang, Michael Bi Mi, and Xinchao Wang. Learning-to-cache: Accelerating diffusion transformer via layer caching. *Advances in Neural Information Processing Systems*, 37:133282–133304, 2024. 2, 7
- [25] Xinyin Ma, Gongfan Fang, and Xinchao Wang. Deepcache: Accelerating diffusion models for free. In *Proceedings of the IEEE/CVF conference on computer vision and pattern recognition*, pages 15762–15772, 2024. 2, 4
- [26] Zehong Ma, Longhui Wei, Feng Wang, Shiliang Zhang, and Qi Tian. Magcache: Fast video generation with magnitude-aware cache. *arXiv preprint arXiv:2506.09045*, 2025. 2, 4, 7
- [27] William Peebles and Saining Xie. Scalable diffusion models with transformers. In *Proceedings of the IEEE/CVF international conference on computer vision*, pages 4195–4205, 2023. 2, 3
- [28] Aditya Ramesh, Prafulla Dhariwal, Alex Nichol, Casey Chu, and Mark Chen. Hierarchical text-conditional image genera-

- tion with clip latents. *arXiv preprint arXiv:2204.06125*, 1(2): 3, 2022. 1
- [29] Robin Rombach, Andreas Blattmann, Dominik Lorenz, Patrick Esser, and Björn Ommer. High-resolution image synthesis with latent diffusion models. In *Proceedings of the IEEE/CVF conference on computer vision and pattern recognition*, pages 10684–10695, 2022. 1, 2, 3
- [30] Olaf Ronneberger, Philipp Fischer, and Thomas Brox. U-net: Convolutional networks for biomedical image segmentation. In *International Conference on Medical image computing and computer-assisted intervention*, pages 234–241. Springer, 2015. 2, 3
- [31] Chitwan Saharia, William Chan, Saurabh Saxena, Lala Li, Jay Whang, Emily L Denton, Kamyar Ghasemipour, Raphael Gontijo Lopes, Burcu Karagol Ayan, Tim Salimans, et al. Photorealistic text-to-image diffusion models with deep language understanding. *Advances in neural information processing systems*, 35:36479–36494, 2022. 1
- [32] Tim Salimans and Jonathan Ho. Progressive distillation for fast sampling of diffusion models. In *The Tenth International Conference on Learning Representations, ICLR 2022, Virtual Event, April 25-29, 2022*. OpenReview.net, 2022. 2, 3
- [33] Yuzhang Shang, Zhihang Yuan, Bin Xie, Bingzhe Wu, and Yan Yan. Post-training quantization on diffusion models. In *Proceedings of the IEEE/CVF conference on computer vision and pattern recognition*, pages 1972–1981, 2023. 2, 4
- [34] Uriel Singer, Adam Polyak, Thomas Hayes, Xi Yin, Jie An, Songyang Zhang, Qiuyan Hu, Harry Yang, Oron Ashual, Oran Gafni, et al. Make-a-video: Text-to-video generation without text-video data. *arXiv preprint arXiv:2209.14792*, 2022. 1
- [35] Jiaming Song, Chenlin Meng, and Stefano Ermon. Denoising diffusion implicit models. *arXiv preprint arXiv:2010.02502*, 2020. 2, 3, 7
- [36] Yang Song, Jascha Sohl-Dickstein, Diederik P. Kingma, Abhishek Kumar, Stefano Ermon, and Ben Poole. Score-based generative modeling through stochastic differential equations, 2021. 2, 3
- [37] Yang Song, Prafulla Dhariwal, Mark Chen, and Ilya Sutskever. Consistency models. *arXiv e-prints*, pages arXiv–2303, 2023. 2
- [38] Ashish Vaswani, Noam Shazeer, Niki Parmar, Jakob Uszkoreit, Llion Jones, Aidan N Gomez, Łukasz Kaiser, and Illia Polosukhin. Attention is all you need. *Advances in neural information processing systems*, 30, 2017. 2
- [39] Patrick von Platen, Suraj Patil, Anton Lozhkov, Pedro Cuenca, Nathan Lambert, Kashif Rasul, Mishig Davaadorj, Dhruv Nair, Sayak Paul, William Berman, Yiyi Xu, Steven Liu, and Thomas Wolf. Diffusers: State-of-the-art diffusion models, 2022. 6
- [40] Team Wan, Ang Wang, Baole Ai, Bin Wen, Chaojie Mao, Chen-Wei Xie, Di Chen, Feiwu Yu, Haiming Zhao, Jianxiao Yang, Jianyuan Zeng, Jiayu Wang, Jingfeng Zhang, Jingren Zhou, Jinkai Wang, Jixuan Chen, Kai Zhu, Kang Zhao, Keyu Yan, Lianghua Huang, Mengyang Feng, Ningyi Zhang, Pandeng Li, Pingyu Wu, Ruihang Chu, Ruili Feng, Shiwei Zhang, Siyang Sun, Tao Fang, Tianxing Wang, Tianyi Gui, Tingyu Weng, Tong Shen, Wei Lin, Wei Wang, Wei Wang, Wenmeng Zhou, Wenten Wang, Wenting Shen, Wenyuan Yu, Xianzhong Shi, Xiaoming Huang, Xin Xu, Yan Kou, Yangyu Lv, Yifei Li, Yijing Liu, Yiming Wang, Yingya Zhang, Yitong Huang, Yong Li, You Wu, Yu Liu, Yulin Pan, Yun Zheng, Yuntao Hong, Yupeng Shi, Yutong Feng, Zeyinzi Jiang, Zhen Han, Zhi-Fan Wu, and Ziyu Liu. Wan: Open and advanced large-scale video generative models. *arXiv preprint arXiv:2503.20314*, 2025. 3
- [41] Changyuan Wang, Ziwei Wang, Xiuwei Xu, Yansong Tang, Jie Zhou, and Jiwen Lu. Towards accurate post-training quantization for diffusion models. In *Proceedings of the IEEE/CVF Conference on Computer Vision and Pattern Recognition (CVPR)*, pages 16026–16035, 2024. 2, 4
- [42] Zhou Wang, A.C. Bovik, H.R. Sheikh, and E.P. Simoncelli. Image quality assessment: from error visibility to structural similarity. *IEEE Transactions on Image Processing*, 13(4): 600–612, 2004. 6
- [43] Felix Wimbauer, Bichen Wu, Edgar Schoenfeld, Xiaoliang Dai, Ji Hou, Zijian He, Artsiom Sanakoyeu, Peizhao Zhang, Sam Tsai, Jonas Kohler, Christian Rupprecht, Daniel Cremers, Peter Vajda, and Jialiang Wang. Cache me if you can: Accelerating diffusion models through block caching. In *Proceedings of the IEEE/CVF Conference on Computer Vision and Pattern Recognition (CVPR)*, pages 6211–6220, 2024. 2
- [44] Chenfei Wu, Jiahao Li, Jingren Zhou, Junyang Lin, Kaiyuan Gao, Kun Yan, Sheng ming Yin, Shuai Bai, Xiao Xu, Yilei Chen, Yuxiang Chen, Zecheng Tang, Zekai Zhang, Zhengyi Wang, An Yang, Bowen Yu, Chen Cheng, Dayiheng Liu, Deqing Li, Hang Zhang, Hao Meng, Hu Wei, Jingyuan Ni, Kai Chen, Kuan Cao, Liang Peng, Lin Qu, Minggang Wu, Peng Wang, Shuting Yu, Tingkun Wen, Wensen Feng, Xiaoxiao Xu, Yi Wang, Yichang Zhang, Yongqiang Zhu, Yujia Wu, Yuxuan Cai, and Zenan Liu. Qwen-image technical report, 2025. 3
- [45] Haocheng Xi, Shuo Yang, Yilong Zhao, Chenfeng Xu, Muyang Li, Xiuyu Li, Yujun Lin, Han Cai, Jintao Zhang, Dacheng Li, et al. Sparse videogen: Accelerating video diffusion transformers with spatial-temporal sparsity. *arXiv preprint arXiv:2502.01776*, 2025. 2
- [46] Yifei Xia, Suhan Ling, Fangcheng Fu, Yujie Wang, Huixia Li, Xuefeng Xiao, and Bin Cui. Training-free and adaptive sparse attention for efficient long video generation, 2025. 2
- [47] Ling Yang, Zhilong Zhang, Yang Song, Shenda Hong, Runsheng Xu, Yue Zhao, Wentao Zhang, Bin Cui, and Ming-Hsuan Yang. Diffusion models: A comprehensive survey of methods and applications. *ACM computing surveys*, 56(4): 1–39, 2023. 2
- [48] Zhuoyi Yang, Jiayan Teng, Wendi Zheng, Ming Ding, Shiyu Huang, Jiazheng Xu, Yuanming Yang, Wenyi Hong, Xiaohan Zhang, Guanyu Feng, Da Yin, Yuxuan Zhang, Weihang Wang, Yean Cheng, Bin Xu, Xiaotao Gu, Yuxiao Dong, and Jie Tang. Cogvideox: Text-to-video diffusion models with an expert transformer, 2025. 3
- [49] Richard Zhang, Phillip Isola, Alexei A. Efros, Eli Shechtman, and Oliver Wang. The unreasonable effectiveness of deep features as a perceptual metric. In *Proceedings of the IEEE Conference on Computer Vision and Pattern Recognition (CVPR)*, 2018. 6

- [50] Wenliang Zhao, Lujia Bai, Yongming Rao, Jie Zhou, and Jiwen Lu. Unipc: A unified predictor-corrector framework for fast sampling of diffusion models. *Advances in Neural Information Processing Systems*, 36:49842–49869, 2023. [2](#), [3](#)
- [51] Xuanlei Zhao, Xiaolong Jin, Kai Wang, and Yang You. Real-time video generation with pyramid attention broadcast. *arXiv preprint arXiv:2408.12588*, 2024. [2](#), [4](#)
- [52] Zangwei Zheng, Xiangyu Peng, Tianji Yang, Chenhui Shen, Shenggui Li, Hongxin Liu, Yukun Zhou, Tianyi Li, and Yang You. Open-sora: Democratizing efficient video production for all, 2024. [3](#)

# InvarDiff: Cross-Scale Invariance Caching for Accelerated Diffusion Models

## Supplementary Material

### 6. Additional Ablations

**Choice of change-rate operator** The adopted rate  $\rho$  compares two successive first-order differences across steps and performs best in our trials. Alternatives that define  $\rho$  by thresholding the MSE relative to the previous step, using cosine distance, or using raw norm ratios attain only limited acceleration at matched quality. This suggests that the chosen rate more faithfully captures module importance for reuse decisions.

**Calibration cost** Two-phase calibration uses one deterministic pass to build the initial plan and a second pass to apply and refine it, so the wall time is roughly twice the time to render the calibration set. With five prompts on FLUX.1-dev, the cost is close to rendering ten full images and is about two minutes on an A800. The calibration prompts are entirely distinct from the GenEval prompts used for evaluation. The resulting plan can be reused for any prompt and seed as long as the number of steps remains the same.

### 7. Threshold Configurations

**Threshold configurations.** Table 4 lists the calibration thresholds used in the main experiments. For DiT-XL/2 we set  $T=50$  and average metrics over 16 random ImageNet classes. For FLUX.1-dev we set  $T=28$  and average over 5 prompts for calibration. The default random seed is 42. The fast and slow columns correspond to the two operating points reported in the main results.

**Preset bundles for speed–quality curves.** Table 5 provides the seven preset module-threshold bundles used to draw the FLUX.1-dev speed–quality curves. The default random seed is 42. For each bundle we keep the six non–step thresholds fixed ( $\tau_{\text{warm-up}}$ ,  $\tau_{\text{dual\_attn}}$ ,  $\tau_{\text{dual\_ff}}$ ,  $\tau_{\text{dual\_context\_ff}}$ ,  $\tau_{\text{single\_attn}}$ ,  $\tau_{\text{single\_ff}}$ ) and sweep the cross-step threshold  $\tau_{\text{step}} \in \{0.40, 0.50, 0.60, 0.70, 0.75\}$  to obtain five operating points. Calibration averages 5 prompts. Points sharing the same bundle index align across polylines in the figure and differ only in  $\tau_{\text{step}}$ .

### 8. Heatmaps under Different Thresholds

We visualize  $(t, l)$  change maps for DiT-XL/2 to show how per–timestep and per–module activations vary across classes. Figure 11 plots, for six randomly sampled ImageNet classes, the MSE and the cosine distance to the previous step for MHSA and FFN. The maps are highly similar across

Table 4. Calibration thresholds used in the main results. DiT-XL/2 uses  $T=50$  and averages over 16 random ImageNet classes. FLUX.1-dev uses  $T=28$  and averages over 5 prompts. Default random seed is 42.

DiT-XL/2 ( $T=50$ )		
Metric	fast	slow
$\tau_{\text{warm-up}}$	0.00	0.00
$\tau_{\text{step}}$	0.63	0.61
$\tau_{\text{attn}}$	0.22	0.20
$\tau_{\text{ffn}}$	0.22	0.20

FLUX.1-dev ( $T=28$ )		
Metric	fast	slow
$\tau_{\text{warm-up}}$	0.10	0.22
$\tau_{\text{step}}$	0.70	0.72
$\tau_{\text{dual\_attn}}$	0.68	0.68
$\tau_{\text{dual\_ff}}$	0.68	0.66
$\tau_{\text{dual\_context\_ff}}$	0.68	0.00
$\tau_{\text{single\_attn}}$	0.68	0.68
$\tau_{\text{single\_ff}}$	0.68	0.62

Table 5. Seven preset module-threshold bundles used for the FLUX.1-dev speed–quality curves. For each bundle,  $\tau_{\text{step}}$  is swept over  $\{0.40, 0.50, 0.60, 0.70, 0.75\}$  to form five operating points. Default random seed is 42.

Bundle	$\tau_{\text{warm-up}}$	$\tau_{\text{dual\_attn}}$	$\tau_{\text{dual\_ff}}$	$\tau_{\text{dual\_context\_ff}}$	$\tau_{\text{single\_attn}}$	$\tau_{\text{single\_ff}}$
1	0.10	0.68	0.68	0.68	0.68	0.68
2	0.10	0.68	0.00	0.00	0.68	0.00
3	0.15	0.68	0.00	0.00	0.70	0.00
4	0.22	0.68	0.66	0.00	0.68	0.62
5	0.22	0.68	0.40	0.00	0.68	0.20
6	0.25	0.68	0.00	0.00	0.68	0.00
7	0.25	0.50	0.00	0.00	0.50	0.00

classes, indicating that the spatio–temporal change patterns are largely class–independent.

To connect this with the reuse criterion, Figure 10 visualizes the  $\rho$  matrices used by our planner. The top rows show six individual classes; the bottom rows show averages over larger class sets. We set the first and last timesteps to one. The matrices exhibit stable bands in time and depth with small class-to-class variation, which supports using a single global quantile to derive thresholds and a cache plan that transfers across classes.

Figures 12 and 13 visualize cache plans after the re-sampling correction on the  $\log_2$ -scaled  $\rho$  matrices. In Figure 12 we fix  $\tau_{\text{step}}=0$  and vary the module thresholds, heatmaps are averaged over 12 randomly sampled classes. White circles mark layer/module reuse and orange circles mark cross-step reuse, with the first and last timesteps set

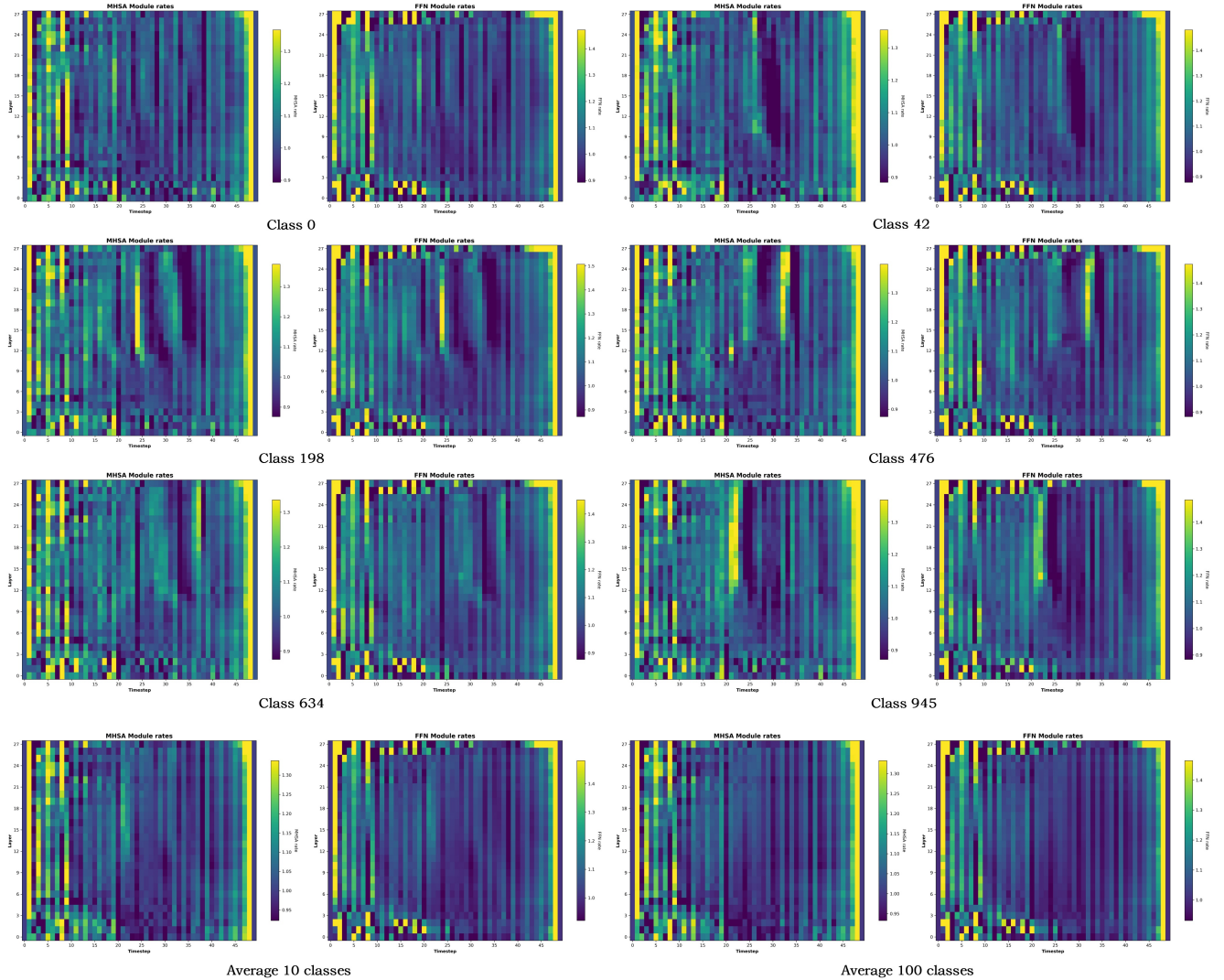


Figure 10. DiT-XL/2 rate matrices  $\rho$  ( $T=50$ ). Top: six random ImageNet classes (each pair shows MHSA and FFN). Bottom: class-averaged maps (left: average over 10 random classes; right: average over 100 random classes). Warmer colors indicate larger  $\rho$ ; the first and last timesteps are fixed to 1. The similar structures across classes and their averages highlight the cross-class stability of  $\rho$ .

to one. Figure 13 stacks multiple rows. The first three rows also average over 12 classes and fix the module thresholds while sweeping  $\tau_{\text{step}}$ . The last row averages over 16 classes and shows two representative operating points.

## 9. Qualitative Results across Operating Points

Figure 14 shows DiT-XL/2 full-compute outputs next to our accelerated results under the same prompts, preserving structure and texture with lower latency. Figures 15 and 16 present FLUX.1-dev across methods and acceleration ratios, where our cache plan maintains visual quality over a broad range of speed-ups.

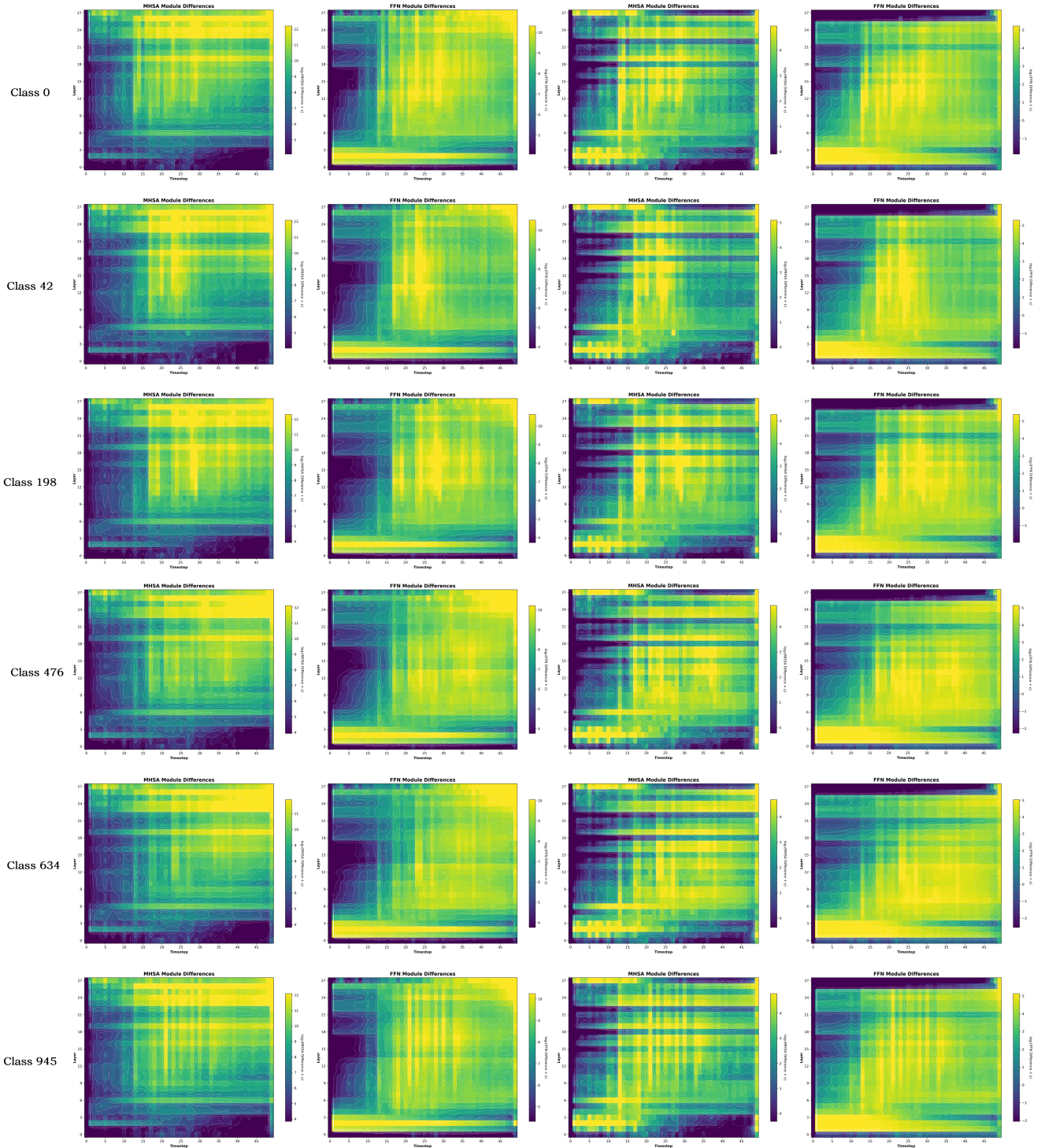


Figure 11. DiT-XL/2 cross-class heatmaps ( $\log_2$  scale,  $T=50$ ). Each row is one of six random ImageNet classes. Columns (left→right): MHSA MSE to previous step, FFN MSE to previous step, MHSA cosine distance, FFN cosine distance. Warmer colors indicate larger change. The first column ( $t=0$ ) is set to 0. The maps are highly similar across classes, indicating stable relative feature differences and supporting class-independent thresholding.

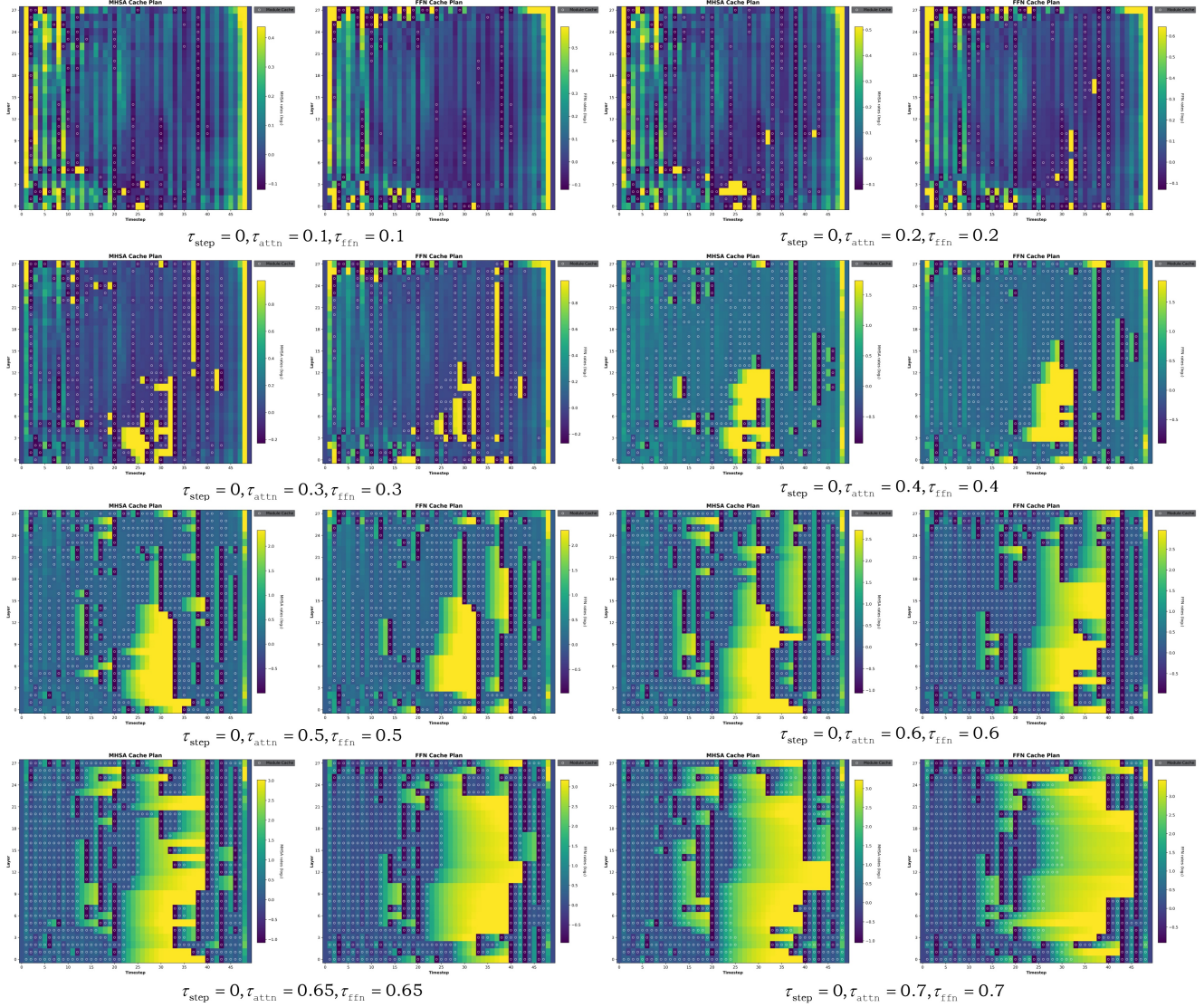


Figure 12. Cache plans after resampling correction ( $\log_2$  scale) on the  $\rho$  matrices with  $\tau_{\text{step}}=0$ . Heatmaps are shown for MHA and FFN. White circles mark layer/module reuse; orange circles mark cross-step reuse; the first and last timesteps are set to one.

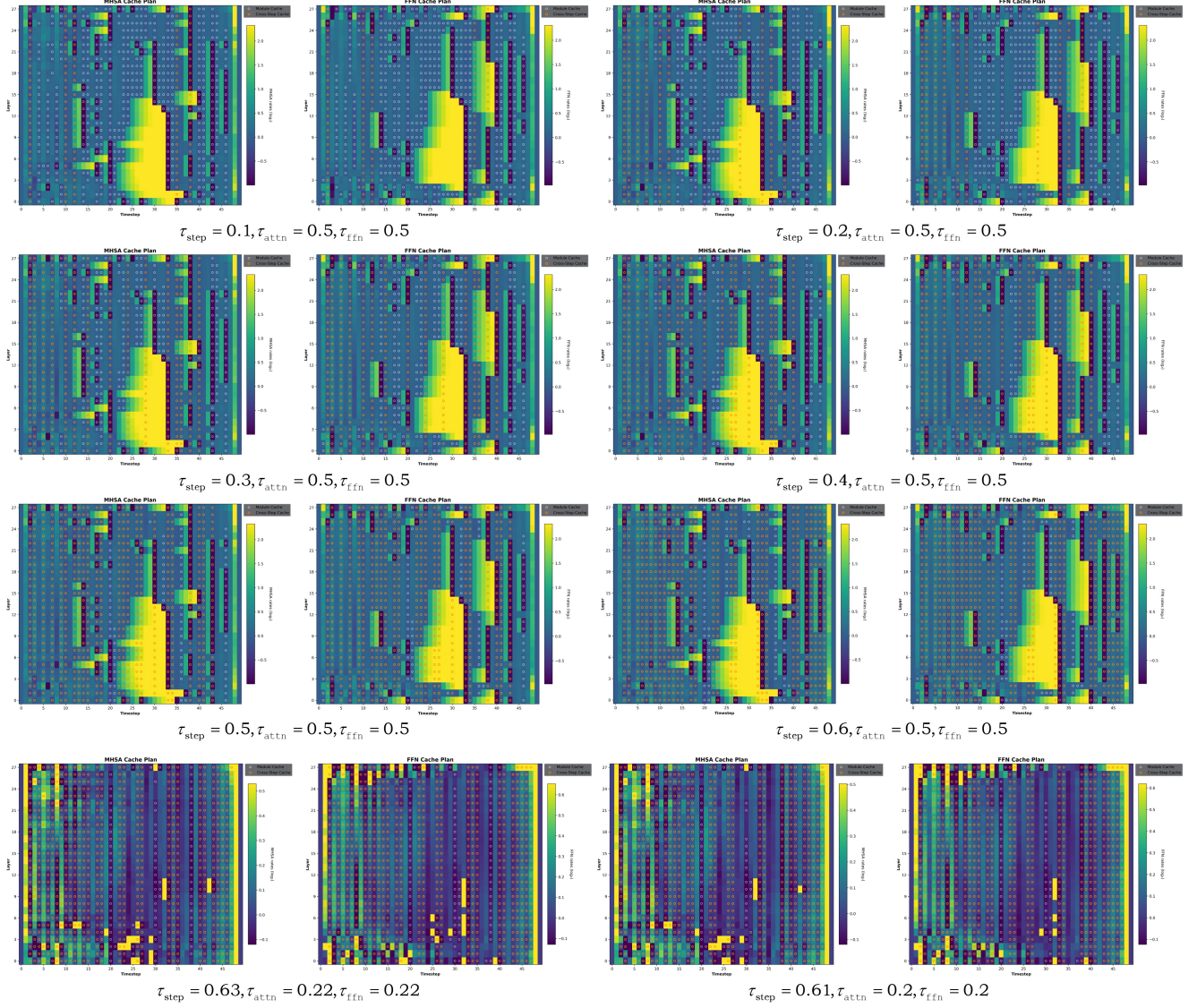


Figure 13. Cache plans after resampling correction ( $\log_2$  scale). The first three rows: fixed module thresholds  $\tau_{\text{dual.attn}} = \tau_{\text{dual.ffn}} = 0.5$  while varying  $\tau_{\text{step}}$ . The last row: two representative operating points. Notation as in Fig. 12.

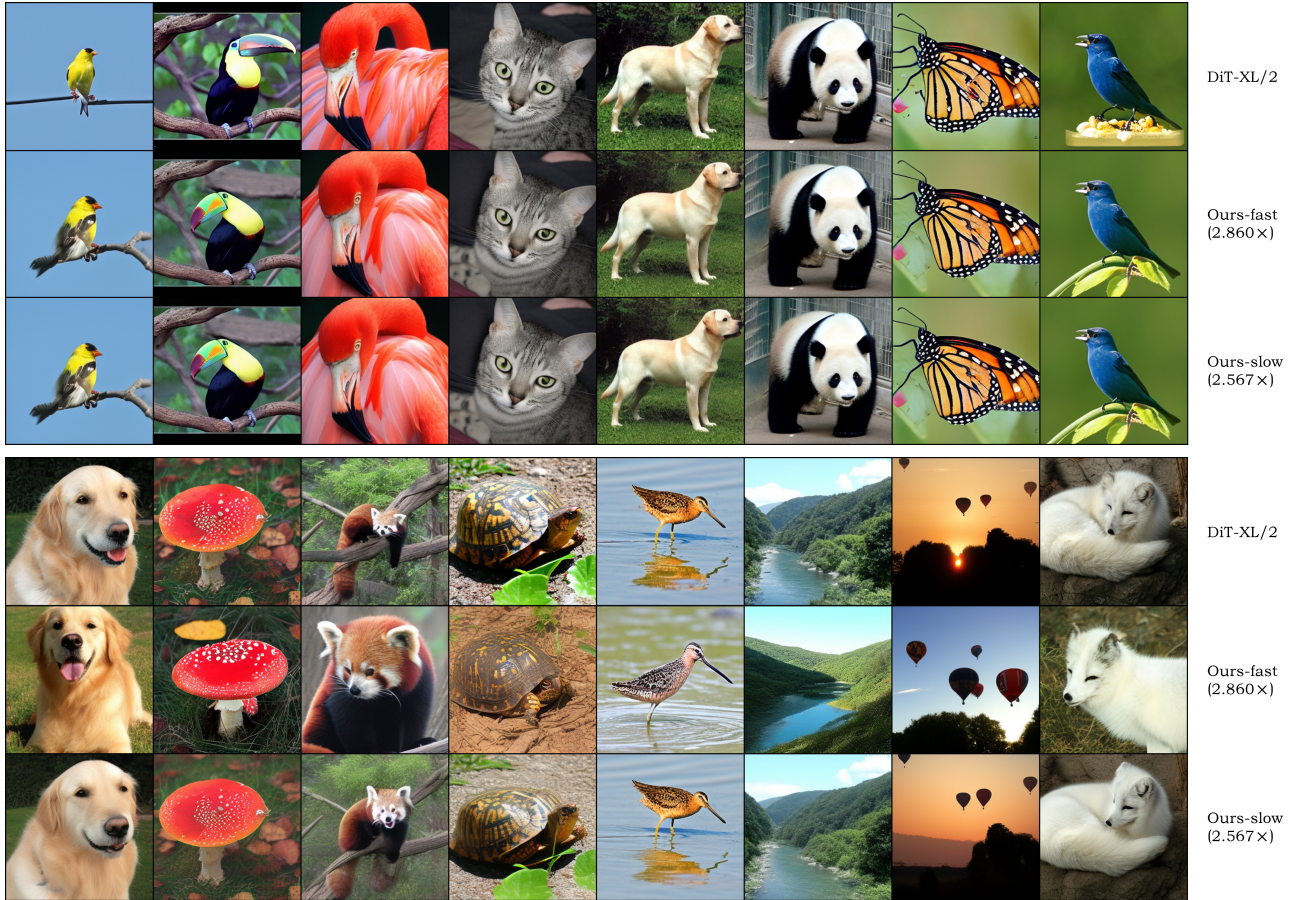


Figure 14. DiT-XL/2 qualitative examples under full compute and our accelerated methods.



Figure 15. FLUX.1-dev qualitative comparison across acceleration methods.



Figure 16. FLUX.1-dev qualitative comparison under different acceleration ratios.